AFRL-SR-AR-TR-09-0271

REPORT DOCUMENTATION PAGE

1. REPORT DATE (DD-MM-YYYY) 08/20/2009	2. REPORT TYPE Final	3. DATES COVERED (From - To) 02/15/2006 – 11/30/2008

4. TITLE AND SUBTITLE	5a. CONTRACT NUMBER
Understanding and Predicting Shockwave and Turbulent Boundary Layer Interactions	FA9550-06-1-0323
	5b. GRANT NUMBER
	5c. PROGRAM ELEMENT NUMBER

6. AUTHOR(S)	5d. PROJECT NUMBER
PI: M. Pino Martin, Princeton University, MAE Department Co-PI: A.J. Smits, Princeton University, MAE Department	5e. TASK NUMBER
	5f. WORK UNIT NUMBER

7. PERFORMING ORGANIZATION NAME(S) AND ADDRESS(ES)	8. PERFORMING ORGANIZATION REPORT NUMBER
Princeton University, D307 ENGINEERING QUADRANGLE OLDEN STREET Princeton, NJ 08544	

9. SPONSORING/MONITORING AGENCY NAME(S) AND ADDRESS(ES)	10. SPONSOR/MONITOR'S ACRONYM(S)
John Schmisseur /NA AFOSR 875 N Randolph Street Arlington, VA	
	11. SPONSOR/MONITOR'S REPORT NUMBER(S)

12. DISTRIBUTION/AVAILABILITY STATEMENT

Distribution A: Approved for Public Release

13. SUPPLEMENTARY NOTES

14. ABSTRACT
Shockwave and turbulent boundary layer interactions produce intense localized pressure loads and heating rates that can have a dramatic influence on the drag and heating experienced by a high-speed vehicle, and can significantly impact fuel mixing and combustion in propulsion systems. The lack of standardized and traceable databases prevents the calibration of computational fluid dynamic models to accurately represent these critical flow phenomena. In this work we accomplished the development and validation against experiments at the same flow and boundary conditions of direct numerical simulations of shock and turbulent boundary layer interactions. We pioneered the development of a unique numerical capability that allows the accurate and detailed three-dimensional turbulence data at a reasonable turn-around time. In turn, parametric studies of fundamental flow physics are feasible, for the first time. By accurate, it is meant that the numerical uncertainty is within the experimental error.

15. SUBJECT TERMS
shockwave, turbulent, boundary, layer, mixing, combustion, calibration, computational, fluid

16. SECURITY CLASSIFICATION OF:			17. LIMITATION OF ABSTRACT	18. NUMBER OF PAGES	19a. NAME OF RESPONSIBLE PERSON John Schmisseur
a. REPORT	b. ABSTRACT	c. THIS PAGE			
					19b. TELEPHONE NUMBER (Include area code) ...5962

2009090 4432

Understanding and Predicting Shockwave and Turbulent Boundary Layer Interactions
M. Pino Martin

PI: M. Pino Martin, Princeton University, MAE Department
Co-PI: A.J. Smits, Princeton University, MAE Department

Other personnel:
Minwei Wu, Princeton University
Matthew Ringuette, Princeton University
Stephan Priebe, Princeton University

ABSTRACT

Shockwave and turbulent boundary layer interactions produce intense localized pressure loads and heating rates that can have a dramatic influence on the drag and heating experienced by a high-speed vehicle, and can significantly impact fuel mixing and combustion in propulsion systems. The lack of standardized and traceable databases prevents the calibration of computational fluid dynamic models to accurately represent these critical flow phenomena.

In this work we accomplished the development and validation against experiments at the same flow and boundary conditions of direct numerical simulations of shock and turbulent boundary layer interactions. We pioneered the development of a unique numerical capability that allows the accurate and detailed three-dimensional turbulence data at a reasonable turn-around time. In turn, parametric studies of fundamental flow physics are feasible, for the first time. By accurate, it is meant that the numerical uncertainty is within the experimental error. By reasonable turn-around time, it is meant that the computational time is comparable to the experimental turn-around-time. The numerical methods, the simulations and their validation against experimental data have been published in the following journal papers:

- Taylor, E.M., Wu, M., and Martín, M.P., "Optimization of Nonlinear Error Sources for Weighted Non-Oscillatory Methods in Direct Numerical Simulations of Compressible Turbulence," *Journal of Computational Physics*, **223**, 384-397, 2007.

- Wu, M., and Martín, M.P., "Direct Numerical Simulation of Shockwave and Turbulent Boundary Layer Interaction induced by a Compression Ramp," *AIAA Journal*, **45**, 4, 879-889, 2007.

- Ringuette, M., Wu, M., and Martín, M.P., "Coherent Structures in DNS of Turbulent Boundary Layers at Mach 3," *Journal of Fluid Mechanics*, **594**, 59-69, 2008

The unsteady motion of STBLI has been analyzed using the DNS data and this work has been published in:

- Wu, M. and Martín, M.P., "Analysis of Shock Motion in STBLI using Direct Numerical Simulation Data," *Journal of Fluid Mechanics*, **594**, 71-83, 2008.

In addition, the data analysis using the DNS of Wu & Martin suggest that low-Reynolds number shock-wave turbulent boundary layer interactions exhibit differences with previous measurements at high Reynolds number. The low Reynolds number effects are due to the greater influence of viscosity, and result in a smaller peak in the RMS of the wall pressure fluctuations, an enriched intermittency of the wall-pressure signal, and a substantially larger separation zone. Unlike previous studies at high Reynolds number, the richer wall-pressure signal of the low-Reynolds number data cannot be used to determine the location of the shock wave. The primary shock wave does not penetrate as deeply into the boundary layer as for the high Reynolds number flows, so it is more accurate to determine the low-Reynolds number shock location in the outer region of the boundary layer. Despite the difference between the low and high Reynolds number data, the low-frequency shock motion (relative to the high-frequency that characterizes the undisturbed boundary layer) reported for high Reynolds number flows, and the turbulence amplification across the interaction region, are not affected by the low Reynolds number condition. These findings have been published in the following journal articles:

- Wu, M., and Martín, M.P., "Direct Numerical Simulation of Shockwave and Turbulent Boundary Layer Interaction induced by a Compression Ramp," *AIAA Journal*, **45**, 4, 879-889, 2007.

- Ringuette, M.J., Wu, M., and Martín, M.P., "Low Reynolds Number Effects in a Mach 3 Shock Turbulent Boundary Layer interaction," *AIAA Journal*, **46**, 7, 2008.

Also, as part of this effort, accurate wall-pressure data for Mach 3 interactions at low Reynolds numbers, accessible to DNS and LES, have been gathered and published in the following journal article:

- Ringuette, M.J., Bookey, P., Wychham, C., Smits, A.J., "Experimental Study of a Mach 3 Compression Ramp Interaction at $Re_\theta = 2400$", *AIAA Journal*, **47**, 2 2009.

TABLE OF CONTENTS

1. Background

1.1. Canonical configurations

The simplest canonical shock and turbulent boundary layer configurations are shown in Fig. 6, namely a compression corner, a reflected shock interaction, and a sharp fin interaction. The flow features for these configurations and our learning from studying these interactions are briefly summarized below.

Compression corner interaction

The compression corner interaction is one of the simplest cases of STBLI that occur in internal and external vehicle flows. This configuration has been extensively studied experimentally by, for example, Settles et al (1979), Kuntz et al. (1987), Smits & Muck (1987), Dolling and Murphy (1983), Ardonceau (1984), and Selig et al. (1989). The early research covers a wide range of turning angles and Reynolds numbers, where the lowest Reynolds number reported is Re_θ = 23,000 (Settles et al, 1978), and the upper Mach number is limited to about 5, corresponding to the experiments by Erengil & Dolling (1991).

We have learned much from the high-Reynolds number experiments. The pressure gradient imposed by the shock can cause the flow to separate in the vicinity of the corner location, and at Mach 2.9 the flow is on the verge of separation with a corner angle of $16°$ (called incipient separation). At $24°$, the time-averaged region of separation spans about 2δ, starting approximately $1.2\,\delta$ ahead of the corner and reattaching at about $0.8\,\delta$ downstream of the corner. Near the line of separation, compression waves merge into a well-defined separation shock, and a second shock forms near the line of attachment (Settles, 1976). Figure 7 illustrates the shock system in a compression corner configuration with increasing compression angle. The corresponding wall pressure distribution shows an inflection point or "plateau" in the region of separation, as shown in Figure 8. Further downstream, the wall-pressure eventually recovers to the inviscid oblique-shock value, but the point where this occurs is located farther downstream with increasing compression angle (Settles et al. 1978). For the $24°$ case, the inviscid value is not recovered before the end of the experimental model is reached, nearly eight boundary layer thicknesses downstream of the corner.

A measure of the upstream influence is the distance from the corner at which the shock presence is first felt. A measure of the streamwise interaction extent is the separation length, being the distance between the separation and reattachment points. These characteristic lengths are determined from time-averaged measurements, and they vary with time due to the highly unsteady motion of the separation shock. The distance over which the separation shock moves increases with turning angle, and at $24°$ it moves about 0.5δ (Selig et al., 1989). The frequency is

typically an order of magnitude lower than any characteristic turbulence frequencies. Thus, the frequency and scale of the shock motion are needed to fully characterize the interaction.

The influence of the compression on the turbulence is an enhanced mixing due to the formation of large-scale eddies (Kuntz et al, 1987) as the incoming boundary layer is driven out of equilibrium. The boundary layer mean flow recovery distance increases with increasing interaction strength (Smits and Muck, 1987; Selig et al., 1989; Ardonceau, 1984; Kuntz et al, 1987). The turbulence levels are strongly amplified across the shock system, and Selig et al., (1989) found that at Mach 2.9 the mass-flux fluctuations increased by more than a factor of four with a 24° turning angle. The flow distortion is also seen in the heat transfer: Evans & Smits (1996) found that the Reynolds analogy factor increased by a factor of three through a 16° interaction, and showed little sign of relaxation downstream of the corner.

In contrast with numerous experimental data, there are few detailed simulations such as DNS (Adams, 2000; Martin & Wu, 2007) and LES and hybrid LES/RANS (Rizzetta & Visbal, 2001; Loginov et al., 2006; Edwards, Choi & Boles, 2008). Recently, a number of experiments (Bookey et al., 2005; Ringuette & Smits, 2007) have been performed at lower DNS- and LES-accessible Reynolds numbers, so that the validation of DNS and LES is possible. From the validated DNS data at low-Reynolds numbers we have learned that greater viscous effects diffuse the shock near the wall, which results in a reduced magnitude of the peak in the RMS of the wall-pressure fluctuations, a richer intermittency of the wall-pressure signal, and a greater spread of the separation zone (Wu & Martin, 2007; Ringuette, Wu & Martin, 2008). While in high Reynolds number experiments the shock motion is inferred from measurements of the wall-pressure, for low Reynolds number flows the single shock does not penetrate as deeply into the boundary layer and the shock location is not well defined in the lower half of the boundary layer. Thus, at low Reynolds numbers, the shock motion is more accurately studied in the outer part of the boundary layer and in the freestream (Wu & Martin, 2007). Low-Reynolds number effects, however, do not alter the characteristic low-frequency unsteadiness of the shock wave and the separation bubble or the magnitude of the turbulence amplification across the interaction (Wu & Martin, 2008; Ringuette, Wu & Martin, 2008).

Experimental data at low Reynolds number and Mach 8 for an 8° compression corner flow have been recently reported (Bookey et al., 2005). There is much to be learned from this flow, even regarding the validity of the strong Reynolds Analogies in the Mach 8 turbulent boundary layer incoming for this interaction configuration.

Reflected shock interaction

This type of interaction has not been studied as extensively as the compression corner case. A review of the reflected shock interaction is given in Delery and Marvin (1986). The strength of the incident shock determines the nature of the interaction. For weak incident shocks, as illustrated in Figure 9, the result is close to the inviscid interaction. The incident shock (C1)

curves progressively as it penetrates the boundary layer due to the decrease in Mach number within the layer. The effect of the incident shock is felt upstream by pressure propagation through the subsonic part of the boundary layer very near the wall. The thickened subsonic region generates outgoing compression waves that coalesce into the reflected shock (C2).

When the incident shock is strong enough, the boundary layer separates and the flow no longer resembles the inviscid case (see Figure 10). Here, the boundary layer separates at point S. Compression waves emanate from the separation region and coalesce into the separation shock (C2). The separation shock intersects the incident shock at H and generates the refracted shocks C3 and C4. Shock C3 enters the boundary layer and reflects off the separated region into an expansion fan. The fan turns the flow towards the wall, which decreases the height of the separation bubble until the flow reattaches at point R. The resulting reattachment compression waves compress the flow gradually.

Green (1970) observed the similarities of the compression corner and reflected wave configurations and pointed out that a compression corner of angle 2θ will produce the same series of compression interactions at separation and reattachment as an incident shock configuration with initial deflection angle θ. In turn, the overall pressure change is the same and the surface pressure distributions are nearly identical (Shang et al, 1976). The scaling of the upstream influence length and separation length is expected to behave similarly to the compression corner interaction. One major difference between the compression corner and the incident shock cases is a larger separation bubble for the incident shock configuration, and, in contrast to a compression corner flow where the separation bubble height is only a small fraction of the incoming boundary layer thickness, the height of the separation region in a reflected wave flow is typically comparable to the incoming boundary layer thickness. Thus, the velocity profiles show significant regions of flow reversal, which result in a significantly increased boundary layer thickness over the separated region (Delery and Marvin, 1986).

More recently, Dupont, Haddad and Debiève (2006) and Dussauge, Dupont and Debiève (2006) studied a reflected shock interaction at $M = 2.3$ and $Re_\theta =6900$ generated by an oblique shock wave with deflection angles varying from $7°$ to $9.5°$. Detailed Mach number, velocity, and fluctuation profiles were obtained. The principal observations agreed with earlier studies on separation length and recovery distance, and significant unsteadiness was observed. The three-dimensional nature of the interaction was also noted, with strong swirling motions appearing to terminate the separation zone in the spanwise direction. Bookey et al. (2005) report experimental data for a $12°$ incident shock on a boundary layer at Mach 2.9 and $Re_\theta=2400$, providing surface pressure distributions and Pitot surveys, and flow visualization using surface oil and CO_2 enhanced filtered Rayleigh scattering (FRS).

Again, there are few detailed simulations such as DNS (Pirozzoli & Grasso, 2006; Priebe, Wu, & Martin 2008) and LES (Garnier, Sagaut, and Deville, 2002). Direct comparison against experiments for this configuration is not possible, where significant three-dimensional effects due to wind tunnel walls are observed experimentally (Bookey et al., 2005; Dussauge, Dupont, & Debiève, 2006). Figure 11 shows surface oil visualizations (Bookey et al. 2005), illustrating the

significant spanwise variation of the flow. DNS including the experimental spanwise length, wind tunnel side wall boundary conditions are not feasible and LES have not yet been validated for these type of flows. Robust DNS methodologies for STBLI, however, have been validated for the compression corner interaction against experiments. Using such methods, Priebe, Wu & Martin (2009) report the detailed DNS data on an incident shock configuration that is generated by a $12°$ wedge in the free stream of a Mach 2.9, $Re_\theta=2390$ turbulent boundary layer. They report on the evolution of the mean and fluctuating flow quantities, the validity of the Strong Reynolds analogies and the characteristic low frequency of shock motion.

Sharp fin induced interaction

A swept-shock interaction is generated when a sharp fin placed at an angle of attack to the incoming flow. Here the oblique shock sweeps across the incoming boundary layer, and strong secondary flows can be produced by the spanwise pressure gradients. As the boundary layer enters the rising pressure, the gradient in Mach number inside the boundary layer will cause the flow near the wall to turn through a greater angle than the flow away from the wall (as long as the pressure gradient dominates). The differential turning leads to a helical secondary flow. Typically, one or more large-scale vortical motions are induced which sweep the low-momentum fluid from the near-wall region of the incoming boundary layer in the direction along the shock (see Figure 12). The high momentum fluid in the outer part of the boundary layer passes over the vortex with a turning angle more typical of the inviscid deflection associated with the shock, and it is then swept close to the wall. The skin friction and heat transfer levels seem largely unaffected by the strong secondary motions, but the values rise sharply in the region closer to the fin where the high momentum fluid "scours" the wall. The turbulence response is not well understood. Very few experimental results are available, but measurements by Tan (see Smits & Dussauge, 2006) suggest that the turbulence levels are strongly amplified, and Tran et al. (1985) found that the shock is unsteady, leading to strong wall-pressure fluctuations. In these respects, three-dimensional interactions appear to be similar to their two-dimensional counterparts, but the detailed response of the turbulence is quite different. In particular, the turbulence amplification and the unsteady pressure loading are weaker.

The shock bifurcates in response to the formation of the helical secondary flow, in a manner very similar to that seen in two-dimensional separated compression-corner flows. There is an initial turning and compression by a well-defined shock, which is slanted forward (the "separation" shock), and a stronger trailing shock, where the two shock structures encompass the large-scale vortical flow. When the flow is viewed along the axis of the helix it appears similar to the cross-section of a two-dimensional separated flow. In that view, a bubble-type separated flow is observed, and the flow characteristics typically scale in conical coordinates. The experiments show that the wall pressure distribution and the total pressure distribution can be collapsed in conical coordinates. One feature that deserves particular attention is the "impinging jet", found in close proximity to the fin itself. As the model by Garg and Settles (1993) makes clear, the jet is formed by high-momentum fluid from the outer regions of the incoming layer (including the freestream) curved toward the surface as the low-momentum fluid near the wall is removed in

the spanwise direction by the main vortical flow. Not surprisingly, the maximum skin-friction and heat-transfer rates occur near the jet impingement location.

These observations are based almost exclusively on relatively low Mach number flows (typically less than 3). Data at higher Mach numbers, relevant to hypersonic flight, are virtually non-existent, except for the recent experimental data of Bookey et al. (2005) reporting surface oil flow visualizations and filtered Rayleigh scattering images for a Mach 8 and Re_θ=3500 STBLI generated by an 8° sharp fin. DNS of sharp fin interactions, even at these low Reynolds numbers, are not feasible, and robust LES are required. Currently, LES of this canonical flow do not exist.

1.2. Shock unsteadiness

One of the key features of shock wave and turbulent boundary layer interactions is the unsteady motion of the shock. The shock motion has a frequency much lower than the characteristic frequency of the incoming boundary layer. The time scale of the low-frequency motion is $O(10\delta/U_\infty$ - 100 $\delta/U_\infty)$ as reported in various experiments such as Dolling & Or (1985), Selig (1988), or Dussauge, Dupont & Debièvc (2006). In contrast, the characteristic time scale of the incoming boundary layer is $O(\delta/U_\infty)$.

The shock unsteadiness has been primarily studied for two-dimensional interactions, where the shock translates in the streamwise direction with translation magnitude of $O(\delta)$ and with smaller wrinkling motion superimposed (Ganapathisubramani, Clemens & Dolling, 2007; Wu & Martin, 2007; Wu, Lempert & Miles, 2000). Figure 13 illustrates such motion. The spanwise wrinkling is caused by the upstream boundary layer structures convecting through the shock (Erengil & Dolling, 1991). Presently, there are two schools of thought that try to explain the cause for the translation motion, namely being given by: (a) the upstream boundary layer, more recently 'superstructures' (Andreopoulos & Muck, 1987; Erengil & Dolling, 1991; Beresh, Clemens, & Dolling, 2002; Ganapathisubramani, Clemens & Dolling, 2007) and (b) the downstream separated flow (Thomas, Putnam & Chu, 1994; Dussauge, Dupont & Debieve, 2006). Recent analysis on validated DNS data of a compression corner employ correlations of shock motion with the upstream and downstream flow to find that the shock motion is mainly correlated with downstream flow dynamics (Wu & Martin, 2008). Similar trends are observed in a reflected shock interaction using analyses on DNS data (Martin, Priebe & Wu, 2008). Dussauge et al. (2006) find that using $St_L = f L/U_\infty$, where L is the streamwise length of the mean separation bubble, experimental data (covering a wide range of Mach numbers and Reynolds numbers and various configurations) can be grouped between St_L= 0.02 and 0.05. This range is consistent with the Strouhal number found in DNS data (Wu & Martin, 2008).

No detailed studies exist regarding heat transfer or real gas effects on shock unsteadiness. In addition, there exist no complete and validated LES data to study the long-term dynamics of shock unsteadiness. Recently, Edwards, Choi & Boles (2008) presents a study of shock motion using a hybrid LES/RANS simulation of a Mach 5 compression corner interaction. However, a

robust and general methodology for shock-capturing in LES of STBLI has not been proven to date.

1.3. *Large eddy simulations*

In the large-eddy simulation (LES) technique, the contribution of the large, energy-carrying structures to momentum and energy transfer is computed exactly, and the effect of the smallest scales of turbulence is modeled. While a substantial amount of research has been accomplished for LES of incompressible flows, applications to compressible flows have been significantly fewer. This is in part due to the limited amount of accurate and detailed data at relevant conditions that have been available in the past to test and develop LES approaches and models.

The traditional LES approach is based on filtering the governing equations and modeling the corresponding subgrid-scale (SGS) terms (Rogallo, 1984; Lesieur, 1996; Piomelli, 1999; Meneveau & Katz, 2000). The resulting SGS models are based on scaling arguments leading to eddy viscosity models, (Smagorinsky, 1963; Moin et al., 1991) physically-based assumptions such as scale similarity (Bardina et al., 1980), and practical add-hoc approximations leading to the monotonically integrated LES approach (MILES) (Boris, 1992; Garnier et al, 1999; Urbin, 2001; Fureby, 2002). In an alternate approach, the unfiltered velocity field is approximated and used to compute the SGS terms in their exact form. Such an approach is used in the estimation model, where an estimate of the unfiltered velocity is obtained by generating subgrid-scales two times smaller than the grid scale through the nonlinear interactions among the resolved scales (Domaradzki, 1997; Domaradzki, 1999; Dubois, 2002). Also, in the approximate deconvolution model (ADM), a mathematical approximation of the unfiltered solution is constructed and used to calculate the nonlinear terms in the filtered governing equations (Stolz, 1999; Stolz, 2001a; Stolz, 2001b; von Kaenel, 2004).

Rizetta and Visbal (2001) perform a LES of flow over a compression corner using a dynamic Smagorinsky model and compared their results to the DNS of Adams (Adams, 2000) and experimental data at higher Reynolds numbers. The Reynolds number discrepancy made it difficult to draw any firm conclusions on the accuracy of the LES. Garnier, Sagaut & Deville (2002) performed a LES of a reflected shock case. Satisfactory comparisons in the mean and fluctuating streamwise velocity with experiments under the same conditions were reported. However, the integration time of the LES was not long enough to study the low frequency shock motion. Loginov et al. (2006) used LES with ADM to simulate a compression corner flow configuration. Comparison with experimental data showed good agreement in the wall-pressure and skin friction distribution. The comparison of the velocity profiles in the streamwise direction also showed promising results. However, the robustness and validity of the ADM model applied to other interaction configurations and flow conditions is still to be verified, given the presence of tunable parameters to achieve the stability and accuracy of the solution.

In the past, we did not have access to detailed experimental or validated DNS solutions. With the refashioned shock-capturing methods that we have developed in our group (see section 3), such limitation does no longer exist. We have access to true DNS data of highly compressible

turbulence interacting with strong shock waves, and using these datasets we can go back and assess the robustness of numerical methodologies and turbulence models for LES, making LES an indisputably reliable tool for the prediction STBLI.

2. Results from this AFOSR sponsored research

As part of a previous AFOSR grant (#FA9550-06-1-0323), we performed a joined numerical and experimental effort with the goal of validating DNS and LES for STBLI. In this regard, detailed experimental data for the three configurations described above were obtained at flow conditions that were accessible to DNS and LES. The experiments and simulations were conducted, respectively, in the Gas Dynamics Laboratory and the CRoCCo Laboratory in Princeton University. For the duration of this grant, we developed shock-capturing weighted-essentially non-oscillatory numerical methods for shock and turbulence interactions, resulting in robust shock-capturing with significantly improved grid convergence properties. Currently, shock-confining filters are being developed to enable robust large-eddy simulations of these flows. The direct numerical simulation data match the experimental data within the experimental uncertainty. In turn, the validated DNS data has been used to develop a greater understanding of the upstream and downstream flow influence on STBLI unsteadiness. Below is a summary of results from previous (past three years and a half) AFOSR sponsored research, regarding numerical methods for DNS, DNS data quality, validation and analyses, and large-eddy simulations.

2.1. *Numerical methods for direct numerical simulations*

Prior to this work, DNS were well-developed for incompressible flows but not for highly-compressible turbulent flows. The simulation of turbulence interacting with shockwaves requires high bandwidth resolving efficiency and robust shock capturing, and great attention must be given to assess the numerical dissipation for accurate solutions. Weighted essentially non-oscillatory (WENO) schemes (Jiang & Shu, 1996) provide robust shock capturing for unsteady flows. With these schemes the numerical flux is computed as a weighted sum of candidate stencils. The WENO technique is best introduced in the context of the one-dimensional advection equation, where the semi-discrete form is

$$\frac{d\hat{u}}{dt} = -\frac{1}{\Delta}\left(\hat{f}_{i+1/2} - \hat{f}_{i-1/2}\right),$$

where $\hat{\circ}$ indicates a discrete quantity and Δ is the mesh spacing. The evaluation of the flux is given as a weighted sum of candidate stencils by

$$\hat{f}_{i+1/2} = \sum_{k=0}^{r} w_k q_k^r,$$

where q_k^r are the candidate flux approximations on the candidate stencils and w_k are the weights assigned to each candidate. Figure 14 shows the candidate stencils for an $r=3$ symmetric WENO approximation. In perfectly smooth regions, the WENO methodology results in an optimal stencil that can be optimized for maximum order of accuracy (Jiang & Shu, 1996) or optimal bandwidth (Weirs & Candler, 1997). If a shock is contained within a stencil, that stencil receives a nearly zero weight, thereby driving the final approximation away from the optimal stencil while avoiding interpolation across shock waves. Martin et al. (2006) show that linearly bandwidth optimized WENO methods (Weirs & Candler, 1997), hereby WENO$_W$, can be used to obtain accurate turbulence results for certain canonical configurations. For isotropic turbulence at incompressible flow conditions, Fig. 15a shows that WENOw schemes can yield grid converged results when using very fine meshes 128^3 grid points, relative to 64^3 grid points for non-shock-capturing schemes. A measure of numerical dissipation for turbulent boundary layers is the skin friction coefficient. For freestream Mach numbers in the range of 3 to 8, Fig. 15b shows that accurate results (within the uncertainty of the van Driest II prediction) can be obtained with WENO$_w$ schemes. Other more stringent problems could not be accurately simulated using simple linearly bandwidth optimized WENO methods. This is the case of shockwave and turbulent boundary layer calculations or LES for which increasing the grid size was not an option. Figures 16a and 16b show the inaccuracy of WENOw for a STBLI in comparison with experiments and a LES of a Mach 4 turbulent boundary layer in comparison to DNS, respectively. The inadequacy of simply linearly optimized WENO methods prompted a series of numerical studies to address the overly dissipative nature of the existing WENO schemes.

The numerical dissipation in WENO comes from two sources: (1) the linear dissipation due to the theoretical bandwidth properties of the optimal stencil; and (2) the non-linear dissipation due to the non-theoretical bandwidth properties of adapted stencils when deviation from the optimal stencil is necessary. The linear source of numerical dissipation was addressed by Weirs & Candler (1997), resulting in the WENO$_w$ schemes. Under AFOSR funding we worked on robust solutions to address the nonlinear numerical dissipation and developed the linear and non-linearly optimized WENO methods (Taylor, Wu & Martin, 2007; Wu & Martin, 2007; Taylor & Martin, 2008). Figure 17 plots DNS results on isotropic turbulence at turbulent Mach number of 1.5 showing that grid convergence is achieved at 64^3 grid points using the new linearly and non-linearly optimized WENO, relative to 128^3 grid points required using simply linearly optimized WENO methods. Figure 18 shows that the new WENO methods result in accurate DNS data (that is within the experimental uncertainty) for shock wave and turbulent boundary layer interactions on affordable grids. We can obtain converged mean and fluctuating quantities in nine days for the compression corner shown in Fig. 18 using the new methods, relative to about a year if were using WENO$_w$. Moreover, the linearly and nonlinearly optimized WENO methods are general and no modifications are necessary to accurately resolve turbulence or perform shock capturing. Using these new methods, we have been able to perform DNS of STBLI, such as those described below, and compressible isotropic turbulence interacting with imposed shock waves such as those in Fig. 2 (Taylor, Grube & Martin, 2008).

2.2. *Validated direct numerical simulation data of STLBI*

Two flow configurations were considered, namely a compression corner interaction with compression angle of $24°$ (Wu & Martin, 2007; Martin & Wu, 2007; Wu & Martin, 2008) and a reflected shock interaction using a free stream flow deflection of $12°$ (Martin, Priebe & Wu, 2008; Priebe, Wu & Martin, 2009).   For both cases, the incoming boundary layer was at Mach 2.9 and Reynolds number based on momentum thickness of 2390, matching the experimental data of Bookey et al. (2005) and Ringuette et al. (2007).

For the compression corner, the mean wall-pressure distribution for the DNS and experimental data (Bookey et al., 2005) for the same configuration and flow conditions is given in Fig. 19a, showing good agreement. The error bars show an estimated experimental error of 5%.   The corner is located at x=0. Figure 19b plots the magnitude of wall-pressure fluctuations from the DNS data and experiments (Ringuette et al., 2007).   There is good agreement between the DNS and experimental data, except that the DNS gives slightly higher magnitude. This is because the synthetically generated turbulence structures in the initial DNS condition produce slightly higher levels of uncorrelated pressure fluctuations, or noise, in the incoming boundary layer.   Thus, the fluctuating wall pressure in the DNS is the sum of the actual value, p'_w, and that due to uncorrelated noise, p'_n, and $\left\langle \left(p'_w + p'_n \right)^2 \right\rangle \approx \left\langle p'^2_w \right\rangle + \left\langle p'^2_n \right\rangle$, since $\left\langle 2 p'_w \, p'_n \right\rangle$ can be neglected. An estimate of the noise level can be obtained using the free stream value, p'_∞, upstream and downstream of the shock interaction region.   The mean squared of the pressure fluctuations is about 0.04% and 0.16% upstream and downstream of the shock, respectively. Taking the square root of these values gives an amplification factor of 2, and an rms noise value of 2% and 4% upstream and downstream of the interaction, respectively.   These estimates give good approximations of the differences between the DNS and experimental data shown in Fig. 19b. The histograms of the wall-pressure signals for the DNS and experimental data at matching conditions are shown in Fig. 20.   The DNS data is low-pass filtered at 50 kHz to match the resolution of the experiment for comparison. Figure 21 plots the pre-multiplied energy spectral density for the wall pressure given by the same DNS and experiments in three streamwise locations: in the undisturbed boundary layer, at the mean separation and at the first peak in the magnitude of wall-pressure fluctuation. U_∞ / δ is 95 kHz for the DNS and 90 kHz for the experiments.   The agreement among the simulation and experimental data is good, with the magnitudes in the DNS data being slightly higher.   For streamwise locations within the separation region the data of both studies show low-frequency peaks at similar locations 0.6-1.2 kHz for DNS and 0.6-0.8 kHz for the experiment.   These low peaks correspond to the characteristic low frequency of the shock motion.   Both numerical and experimental spectra exhibit peaks at high frequencies (of order 105 kHz), with disagreement between the peak locations of the DNS and the experiments. This is due to a combination of effects, namely the low-pass filtering of the experimental signal, which determines the maximum frequency resolution at about 17 kHz (Ringuette et al., 2007), and the effect of the characteristic forcing frequency imposed by the rescaling method at about 21 kHz (Martin & Wu, 2007).

Bookey et al. (2005) gathered experimental data for the reflected shock case for the same incoming boundary layer flow conditions and free stream deflection angle as those used in the

DNS. They found significant three-dimensional effects imposed by the side walls in the experiment. Figure 11 shows surface oil visualizations from the experiment and a schematic drawing of the near-wall flow pattern. The three-dimensionality imposed by the experimental side walls affects the flow downstream of the separation point and the wall-pressure. The computer power required to simulate the entire experimental span and the side walls renders such calculations impossible today. Thus, comparing the DNS and experiment data is not sensible since the configurations are different. The numerical method is general and robust and has been applied to a variety of shock interaction problems over a range of conditions without modification (Wu & Martin, 2007; Taylor, Wu & Martin, 2007; Taylor, Grube & Martin, 2007), allowing us to proceed with confidence in the calculation and analysis of the DNS data for the reflected shock interaction. Figure 12a plots the wall-pressure signals for the DNS data at different streamwise locations, incoming boundary layer, mean separation point, and inside the separated region. The signals resemble those for the compression corner case. Figure 12b plots the pre-multiplied energy spectral density for the wall pressure signals. The peaks associated with the characteristic low and high frequencies are about 0.15-0.5 kHz and 17-40 kHz, respectively. The scaling proposed by Dussauge et al, $St_L = f L/U_\infty$, together with the DNS data for the compression corner can be used to obtain a theoretical estimate for the characteristic low-frequency of shock motion in the reflected shock case. Figure 23 plots the skin friction coefficient for the compression corner and reflected shock case DNS data, with x=0 at the separation point. The size of the separation region for the reflected shock case is about 1.82 times that of the compression corner case. Using the scaling, the low frequency for the reflected shock case is 1/1.82 that for the compression corner, or about 0.3-0.7 kHz, which is close to the values given by the DNS.

The DNS data analysis of the upstream and downstream influence on the shock unsteadiness for the compression corner and reflected shock cases above indicates that the shock unsteadiness is driven by the downstream flow (Martin & Wu, 2007; Wu & Martin, 2008; Martin, Priebe & Wu, 2008).

2.3. Large-eddy simulation

In the past, we implemented and validated SGS mixed models for compressible flows in isotropic turbulence and turbulent boundary layers (Martin, Piomelli & Candler, 2000; Martin, 2000) and a LES capability in generalized curvilinear coordinates was validated (Martin et al. 2000). More recently, we added the ADM approach to our LES code (Grube, Taylor & Martin, 2007). Despite our LES capability, it was our choice not to perform LES of STBLI until we had validated our ability to perform robust DNS of STBLI and satisfactory validation of the data against experiments had been achieved. Recently, we became confident that we had satisfied this constraint and we moved forward in the development and assessment of robust LES methodologies and models. In particular, we focused our efforts in assessing the need and developing shock-confining filters for LES of turbulence interacting with shock waves (Taylor, Grube & Martin, 2007; Grube, Taylor & Martin, 2007), as well as details regarding commutative errors (Grube & Martin, 2009).

With the exception of static eddy viscosity models, most turbulence models employed in LES require explicit application of filtering operations, sometimes more than once during a given time advancement stage. Dynamic (Germano et al., 1991; Moin et al., 1991), scale-similarity (Bardina et al., 1980), and mixed (Speziale et al., 1988; Vreman, Geurts & Kuerten, 1994) models rely on filtering to identify the smallest resolved length scales; and ADM relies on the iterative application of filtering to approximately de-filter the flow solution. Therefore the calculations of the unclosed terms of the filtered Navier-Stokes equations, and in turn the global dynamics of the simulated fluid flow, are directly affected by the choice of filtering technique. In the vicinity of shocks (or other discontinuities), part of the filter stencil may lie across a shock, and in general this filtering will cause smearing of the shock and/or the creation of spurious oscillations on either side of the shock. In order to avoid filtering across shocks, we have developed a shock-confining filtering (SCF) technique which adapts its coefficients in response to the local smoothness of the flow solution (Grube, Taylor & Martin, 2007). Figure 24 illustrates schematically the desired behavior of an SCF, namely discontinuities are unaffected, but smooth regions are filtered. In Taylor, Grube & Martin (2007), we use DNS data of shock/isotropic-turbulence interaction to perform preliminary testing of the shock-confining filters against linear filters. We find that linear filtering consistently causes streamwise profile (across the shock) data to exhibit anomalies immediately downstream of the main shock, which is indicative of non-negligibly altered global flow dynamics. We also find that these can be consistently avoided by the application of shock-confining filters.

In LES models using ADM, a relaxation parameter is introduced in an attempt to filter the spurious oscillations that are generated during the linear filtering operation across a shock wave. Figure 25 shows the performance of ADM on laminar shock tube flow using central schemes as in Stolz & Adams (2001). The generation of spurious oscillations without the relaxation parameter, and the unsuccessful removal of oscillations by the relaxation parameter are apparent. Figure 26 shows the behavior of ADM with WENO$_w$ not employing SCF, giving slightly better results than ADM with central schemes. Finally, Fig. 27 shows the combination of linearly and non-linearly optimized WENO with SCF for ADM, successfully removing spurious oscillations and robustly performing shock capturing.

In conclusion, we have developed shock confining filters that will potentially enable robust (stable without tuning parameters) LES of STBLI. We have tested these filters a priori using DNS data of shock/isotropic-turbulence interaction, and a posteriori on decaying compressible isotropic turbulence and laminar shock-tube calculations. Further testing a posteriori remains to be done on shock/isotropic-turbulence interaction and STBLI. In addition, further assessment of the linear and non-linearly optimized WENO methods is necessary for LES resolution in STBLI to render such LES methods general and robust.

REFERENCES

1. Adams, N.A. (2002) "Direct Numerical Simulation of the Turbulent Boundary Layer along a Compression Ramp at Mach 3 and Re_0 1685," *Journal of Fluid Mechanics*, **420**, 47-83.
2. Andreopoulos, J., and Muck, K.C. (1987) "Some new aspects of the shockwave/boundary layer interaction in compressible-ramp flows," *Journal of Fluid Mechanics,* **180**, 405-428.
3. Ardonceau, P.L. (1984) "The Structure of Turbulence in a Supersonic Shockwave/Boundary Layer Interaction," *AIAA Journal* **22**, 9 1254-1262.
4. Bardina, J., Ferziger, J.H., Reynolds, W.C. (1980) "Improved subgrid-scale models for large eddy simulation," *AIAA Paper 1980-1357.*
5. Beresh, S.J., Clemens, N.T., and Dolling, D.S. (2002) "Relationship between upstream turbulent boundary layer velocity fluctuations and separation shock unsteadiness," *AIAA J.* **40**, 2412-2423.
6. Bookey, P., Wyckham, C., Smits, A.J., and Martin, M.P. (2005) "New Experimental Data of STBLI at DNS/LES Accessible Reynolds Numbers, *AIAA Paper No. 2005-0309.*
7. Bookey, P. (2005) "An Experimental Study of Shock/Turbulent Boundary Layer Interaction at DNS Accessible Reynolds Numbers," Master of Science in Engineering *Thesis, Princeton University.*
8. Boris, J., Grinstein, F., Oran, E., and Kolbe, R. (1992) "New insights into large-eddy simulations," *Fluid Dynamics Research* **10**.
9. Delery, J. and Marvin, J.G. (1986) "Shockwave Boundary Layer Interactions," AGARD-AG-280.
10. Dolling, D. and Murphy, M. (1983) "Unsteadiness of the Separation Shockwave in a Supersonic Compression Ramp Flowfield," *AIAA Journal* **21**, 12.
11. Dolling, D.S. and Or, C.T. (1985) "Unsteadiness of the shock wave structure in attached and separated compression-ramp flows," *Experiments in Fluids, 3, 24-32.*
12. Domarazdki, J. and Saiki, E. (1997) "A subgrid-scale model based on the estimation model of unresolved scales of turbulence," *Physics of Fluids,* **9**.
13. Domarazdki, J. and Loh, K. (1999) "The subgrid-scale estimation model in the physical scale representation," *Physics of Fluids,* **11**.
14. Duan, L., and Martin, M.P., "Validation of a DNS code for wall-bounded turbulence including finite-rate reactions and surface catalysis", *AIAA Paper 2008-0645.*
15. Dubois, T., Domarazdki, J., and Honein, L. (2002) "The subgrid-scale estimation model applied to large-eddy simulations of compressible turbulence," *Physics of Fluids,* **14**.
16. Dupont, P,. Haddad, C. and Debiève, J.F., (2005) "Space and Time Organization in a Shock Induced Separated Boundary Layer," to appear *Journal of Fluid Mechanics*.
17. Dussauge, J.P., Dupont, P. and Debieve, J.F. (2006) "Unsteadiness in shockwave boundary layer interactions with separation," *Aerospace Science and Technology,* **10**.

18. Edwards, J.R., Choi, J.-I., and Boles, A. (2008) "Large-Eddy/Reynolds-Averaged Navier-Stokes Simulation of a Mach 5 Compression-Corner Interaction", *AIAA Journal*, **46**, 4, 2008.

19. Erengil, M.E., and Dolling, D.S., "Unsteady Wave Structure near Separation in a Mach 5 Compression Ramp Interaction," AIAA Journal, Vol. 29, No. 5,1991, pp. 728-735.

20. Evans, T. & Smits, A.J. (1996) "Measurements of the Heat Transfer in a Shock Wave Turbulent Boundary Layer Interaction," *Experimental Thermal and Fluid Science*, **12**, 87-97.

21. Fureby, C. and Grinstein, F. (2002) "Large-eddy simulation of high Reynolds number free and wall-bounded flows," *Journal of Computational Physics*, **181.**

22. Ganapathisubramani, B., Clemens, N.T., and Dolling, D.S. (2007) "Effects of upstream boundary layer on the unsteadiness of shock induced separation," *Journal of Fluid Mechanics*, **858**, 369-394.

23. Garg, S. & Settles, G.S. (1993) "Wall Pressure Fluctuations Beneath Swept Shock/Boundary Layer Interactions," *AIAA Paper No. 1993-0384.*

24. Garnier, E., Mossi, M., Sagaut, P., Compte, P., and Deville, M. (1999) "On the use of shock-capturing schemes for large-eddy simulation," *Journal of Computational Physics*, **153.**

25. Garnier, E., Sagaut, P., and Deville, M. (2002) "Large eddy simulation of shock boundary layer interaction, " *AIAAJ* **40**, 1935-1944.

26. Germano, M., Piomelli, U., Moin, P., and Cabot, W.H. (1991) "A dynamic subgrid deale eddy viscosity model," *Physics of Fluids*, **3**, 1760-1765.

27. Green, J.E. (1970) "Interaction Between Shockwaves and Turbulent Boundary Layers," *Progress in Aerospace Sciences*, **11**.

28. Grube, N., Taylor, E.M., and Martin, M.P. (2007) "Assessment of WENO methods with shock-confining filtering for LES of compressible turbulence", *AIAA Paper 2007-4198.*

29. Grube, N., and Martin, M.P. (2009) "Large- Eddy Simulation of Shock- wave/Isotropic Turbulence Interaction", *AIAA Paper Number 2009-4165*, 39th AIAA Fluid Dynamics Conference, San Antonio, Texas.

30. Jiang, G., and Shu, C. (1996) "Efficient implementation of weighted ENO schemes," *Journal of Computational Physics*, **126**, 202-228.

31. Kuntz, D.W., Amatucci, V.A., and Addy, A.L. (1987) "Turbulent Boundary Layer Properties Downstream of .the Shockwave/Boundary-Layer Interaction," *AIAA Journal* **25**, 5, 668-675.

32. Lempert, W.R., Wu, and Miles, R.B. (1997) "Filtered Rayleigh scattering measurements using a MHz rate pulse-burst laser system," *AIAA Paper 1997-0500.*

33. Lesieur, M., and Metais, O. (1996) "New trends in large-eddy simulation of turbulence," *Annual Review of Fluid Mechanics*, **28**.

34. Loginov, M.S., Adams, N.A. and Zheltovodov, A.A. (2006) "Large-eddy simulation of shockwave-turbulent-boundary-layer interaction," *Journal of Fluid Mechanics*, **565**, 135-169.

35. Maclean, M., Wadhams, T., Holden, M., and Johnson, H. (2008) "A computational analysis of ground test studies of the HIFiRE-1 transition experiment," *AIAA Paper No. 2008-0641*.

36. Martin, M.P., Piomelli, U., and Candler, G.V. (2000) "Subgrid-Scale Models for Compressible LES," *Theoretical and Computational Fluid Dynamics*, **13**, 5, 361-376.

37. Martin, M.P. (2004) ``DNS of Hypersonic Turbulent Boundary Layers,'' *AIAA Paper No. 2004-2337*.

38. Martin, M.P. (2007) "DNS of Hypersonic Turbulent Boundary Layers. Part I: Initialization and Comparison with Experiments," *Journal of Fluid Mechanics*, **570**, 347-364, 2007.

39. Martin, M.P. and Candler, G.V. (1998) "Effect of Chemical Reactions on Decaying Isotropic Turbulence," *Physics of Fluids*, **10**, 7, 1715–1724.

40. Martin, M.P. and Candler, G.V. (1999) "Subgrid-Scale Model for the Temperature Fluctuations in Reacting Hypersonic Turbulent Flows," *Physics of Fluids*, **11**, 9, 2765-2771.

41. Martin, M.P. and Candler, G.V. (2001) "Temperature Fluctuation Scaling in Reacting Turbulent Boundary Layers," *AIAA Paper No. 01–2717, 31st*.

42. Martin, M.P. and Candler, G.V. (2006) "A Parallel Implicit Method for the Direct Numerical Simulation of Compressible Flows," *Journal of Computational Physics*, **215**, 1, 153-171.

43. Martin, M.P., Priebe, S., and Wu, M. (2008) "Upstream and downstream influence on the unsteadiness of STBLI using DNS data in two configurations", *AIAA Paper 2008-0719, 46th*.

44. Martin, M.P., Taylor, E.M., Wu, M., and Weirs, V.G. (2006) "A Bandwidth-Optimized WENO Scheme for the Direct Numerical Simulation of Compressible Turbulence," *Journal of Computational Physics*, **220**, 1, 270-289.

45. Martin, M.P., and Wu, M., (2007) "Upstream and downstream influence on the unsteadiness of STBLI using DNS data", Proceedings of the IUTAM Symposium on Unsteady Separated Flows and their Control, Corfu, Greece.

46. Martin, M.P., Weirs, G., Candler, G.V., Piomelli, U., Johnson, H., and Nompelis, I., (2000) "Toward the large-Eddy Simulation Over a Hypersonic Elliptical Cross-Section Cone," *AIAA Paper No. 2000-2311*.

47. Meneveau, C., and Katz, J. (2000) "Scale-invariance and turbulence models for large-eddy simulations," *Annual Review of Fluid Mechanics*, **32**.

48. Moin, P., Squires, K., Cabot, W., and Lee, S. (1991) "A dynamic subgrid-scale model for compressible turbulence and scalar transport," *Physics of Fluids,* **11**.

49. Muck, K.C., Andreopoulos, Y. and Dussauge, J.P. (1988) "Unsteady Nature of Shock Wave/Turbulent Boundary Layer Interaction," *AIAA Journal,* **26**, 179-197.

50. Piomelli, U. (1999) "Large-eddy simulation: Achievements and challenges," *Progress in Aerospace Sciences,* **34**.

51. Pirozzoli, S. and Grasso, F. (2006) "Direct numerical simulation of impinging shockwave/turbulent boundary layer interaction at M=2.25", *Physics of Fluids*, **18**.

52. Priebe, S., Wu, M., and Martin, M.P. (2008) "Direct numerical simulation of a reflected shockwave and turbulent boundary layer interaction," *AIAA Journal*, **47**, 5, 2009.

53. Ringuette, M. and Smits, A.J. (2007) "Wall-pressure measurements in a Mach 3 shockwave turbulent boundary layer interaction at a DNS accessible Reynolds number," *AIAA paper 2007-4113*.

54. Ringuette, M.J., Wu, M., and Martin, M.P., "Low Reynolds Number Effects in a Mach 3 Shock Turbulent Boundary Layer interaction," accepted for publication in *AIAA Journal*, 2008.

55. Rizzetta, D.P. & Visbal, M.R. (2001) "Large-Eddy Simulation of Supersonic Compression Ramp Flow by High-Order Method," *AIAA Journal* **39**, 2283-2292.

56. Rogallo, R., and Moin, P. (1984) "Numerical simulation of turbulent flows," *Annual Review of Fluid Mechanics,* **28**.

57. Schülein, E. (2006) "Skin friction and heat flux measurements in shock/boundary layer interaction flows," **44**, 1732-1741.

58. Selig, M.S. (1988) "Unsteadiness of Shockwave/Turbulent Boundary Layer Interactions in Dynamic Control," Ph.D. Thesis, Princeton University.

59. Selig, M.S., Muck, K., Dussauge, J., and Smits, A.J. (1989) "Turbulent Structure in a shock Wave/Turbulent Boundary Layer Interaction," *AIAA Journal*, **27**, 7 862-869.

60. Settles, G.S., Bogdonoff, S.M., and Vas, I.E. (1976) "Incipient Separation of a Supersonic Turbulent Boundary Layer at High Reynolds Number," *AIAA Journal* **14**, 1 50-56.

61. Settles, G.S., Fitzpatrick, T.J., and Bogdonoff, S.M. (1978) "A Detailed Study of Attached and Separated Compression Corner Flowfields in High Reynolds Number Supersonic Flow," *AIAA Paper No. 1978-1167*.

62. Settles, G., Vas, I., and Bogdonoff, D. (1979) "Detailed Study of Attached and Separated Compression Corner Flowfields in High Reynolds Number Supersonic Flow," *AIAA* Journal **17**, 6.

63. Shang, J.S., Hankey Jr., W.L., and Law, C.H. (1976) "Numerical Simulation of Shockwave/Turbulent Boundary Layer Interaction," *AIAA Journal* **14**, 10 1451-1457.

64. Smagorinsky, J. (1963) "General circulation experiments with the primitive equations. I. The basic experiment," *Monthly Weather Review*, **91**.

65. Smits, A.J., and Dussage, J.-P. (1996) "Turbulent Shear Layers in Supersonic Flow," American Institute of Physics Press, Woodbury, New York.

66. Smits, A.J., and Muck, K. (1987) "Experimental Study of Three Shockwave/Turbulent Boundary Layer Interactions," *Journal of Fluid Mechanics*, **182**, 291-314.

67. Speziale, C. Erlebacher, G., Zang, T., and Hussaini, M. (1988) "The subgrid-scale modeling of compressible turbulence, " *Physics of Fluids*, **31**.

68. Stolz, A. and Adams, N. (1999) "An approximate deconvolution procedure for large-eddy simulation," *Physics of Fluids,* **14**.

69. Stolz, A. and Adams, N. (2001) "An approximate deconvolution procedure for large-eddy simulation with application to incompressible wall-bounded flows," *Physics of Fluids,* **13**.

70. Stolz, A., Adams, N., and Kleiser, L. (2001) "The approximate deconvolution model for LES of compressible flows and its application to shock-turbulent-boundary-layer interaction," *Physics of Fluids,* **13**.

71. Taylor, E.M., Grube, N., and Martin, M.P. (2007) "Evaluation of traditional and shock-confining LES filters using data of compressible turbulence", *AIAA Paper 2007-419*.

72. Taylor, E.M., and Martin, M.P., "Synchronization of Weighted Essentially Non-Oscillatory Methods," Accepted for publication in *Communications in Computational Physics*.

73. Taylor, E.M., Wu, M., and Martin, M.P. (2007) "Optimization of Nonlinear Error Sources for Weighted Non-Oscillatory Methods in Direct Numerical Simulations of Compressible Turbulence," *Journal of Computational Physics*, **223**, 384-397.

74. Thomas, F.O., Putnam, C.M., and Chu, H.C. (1994) "On the mechanism of unsteady shock oscillation in shock wave. Turbulent boundary layer interactions," *Experiments in Fluids*, **18**, 68-81.

75. Tran, T.T., Tan, D.K.M., and Bogdonoff, S.M. (1985) "Surface Pressure Fluctuations in a Three-Dimensional Shockwave/Turbulent Boundary Layer Interaction at Various Shock Strengths," *AIAA Paper No. 1985-1562*.

76. Urbin, G. and Knight, D. (2001) "Large-eddy simulation of a supersonic boundary layer using an unstructured grid," *AIAA Journal,* **39**.

77. von Kaenel, R., Kleiser, L., Adams, N., and Vos, J. (2004) "Large-eddy simulation of shock turbulence interaction," *AIAA Journal*, **42**.

78. Vreman, B., Geurts, B., and Kuerten, H. (1997) "Large-eddy simulation of the turbulent mixing layer," *Journal of Fluid Mechanics*, **339**.

79. Weirs, V.G. and Candler, G.V. (1997) "Optimization of weighted ENO schemes for DNS of compressible turbulence," *AIAA Paper 1997-1940*.

80. Wu, M., and Martin, M.P., "Direct Numerical Simulation of Shockwave and Turbulent Boundary Layer Interaction induced by a Compression Ramp," *AIAA Journal*, **45**, 4, 879-889, 2007.

81. Wu, M. and Martin, M.P., "Analysis of Shock Motion in STBLI using Direct Numerical Simulation Data," *Journal of Fluid Mechanics,* **594**, 71-83, 2008.

82. Xu, S. and M.P. Martin, ``Assessment of Inflow Boundary Conditions for Compressible Turbulent Boundary Layers,'' Physics of Fluids 16, pp. 2623 (2004). Also AIAA Paper No. 2003-3963, June 2003.

83. Zheltovodov, A.A. (2004) "Advances and Problems in Modeling of Shockwave Turbulent Boundary Layer Interactions," *Proceedings of the International Conference on the Methods of Aerophysical Research*, Novosibirsk, Russia, Part I, 149-157.

FIGURES
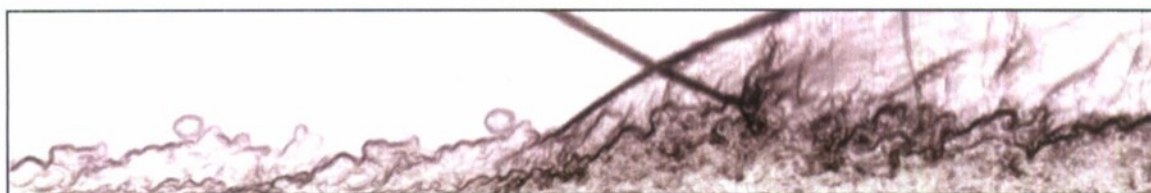
Figure 1: DNS data (Martin, Priebe & Wu, 2008) of a reflected shock interaction. Incoming boundary layer at Mach 2.9 and Re$_\theta$=2390, shock induced by a 12° wedge in the free stream. Magnitude of density gradients is shown.
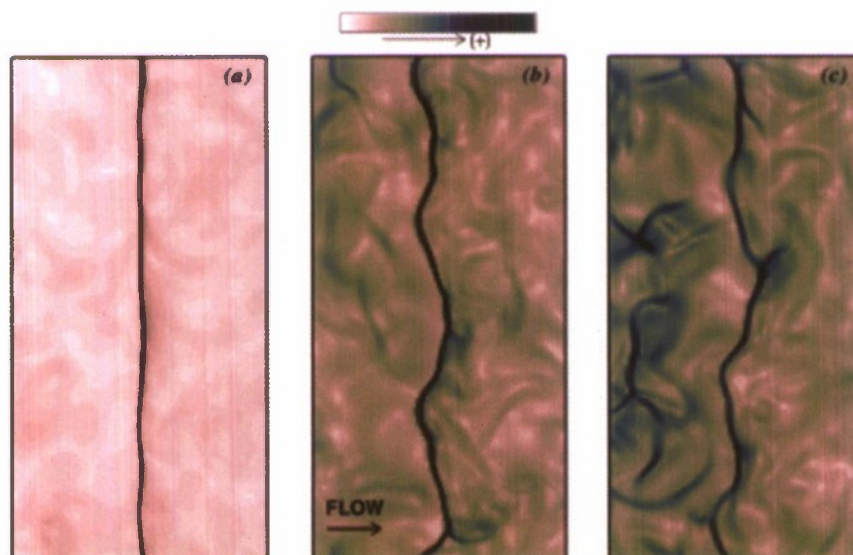
Figure 2. Contours of normalized density gradient $\left|\nabla\rho\right|/\left\langle\rho\right\rangle$ on instantaneous cross-sections of DNS of tested shock/isotropic-turbulence interaction configurations. (a) M=1.5, Re$_{\lambda o}$=25, M$_{to}$=0.2; (b) M=2.0, Re$_{\lambda o}$=35, M$_{to}$=0.7; (c) M=2.0, Re$_{\lambda o}$=35, M$_{to}$=1.3. From Taylor, Grube & Martin (2007).
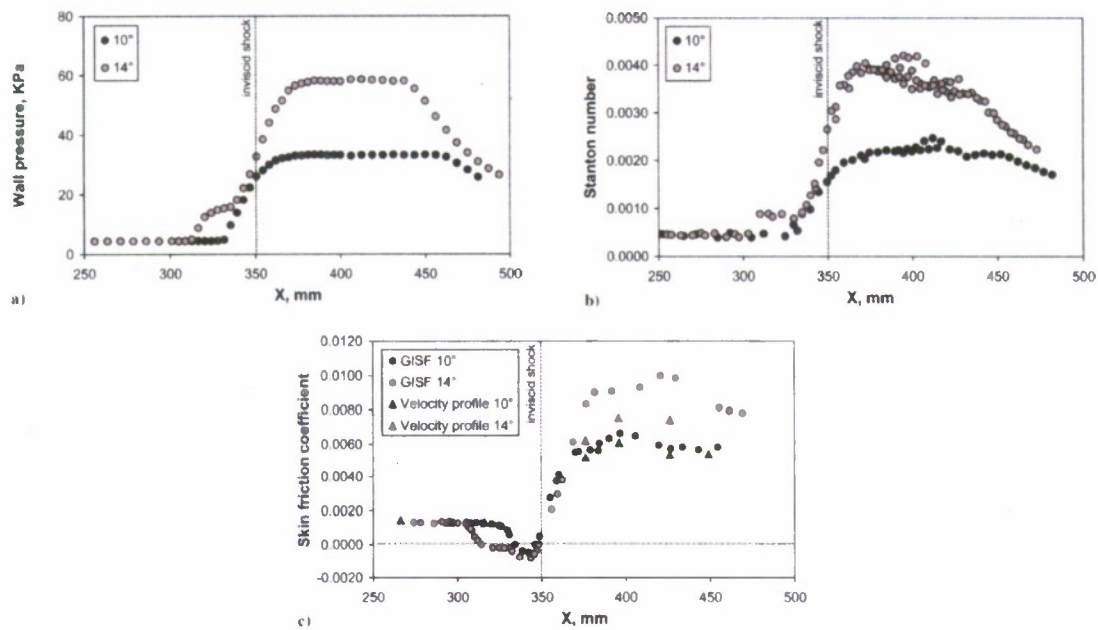
Figure 3: Experimental data (adapted from Schülein, 2006) on two swept shock interactions generated by a sharp fin on a Mach 5 and Re/m=5-50x10^6 boundary layer.
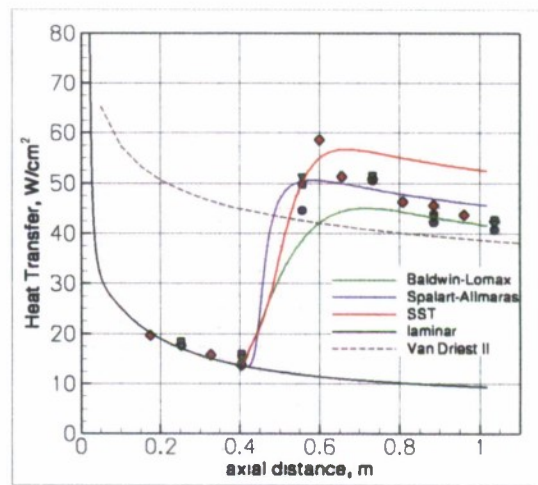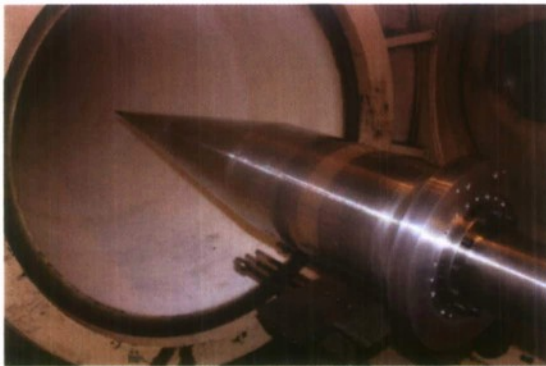
Figure 4: Heat transfer as predicted by various RANS calculations on the blunt cone forebody of the HIFiRE-1 vehicle (MacLean, Wadhams & Holden, 2008).
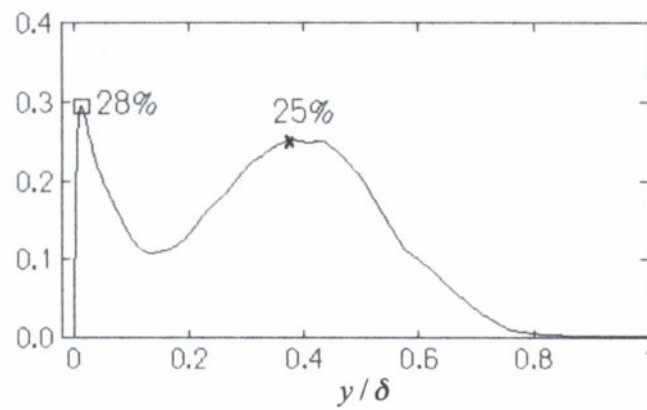
Figure 5: magnitude of species fluctuations in a reacting Mach 4 boundary layer at $Re_\theta=9480$ (from Martin & Candler, 2001).
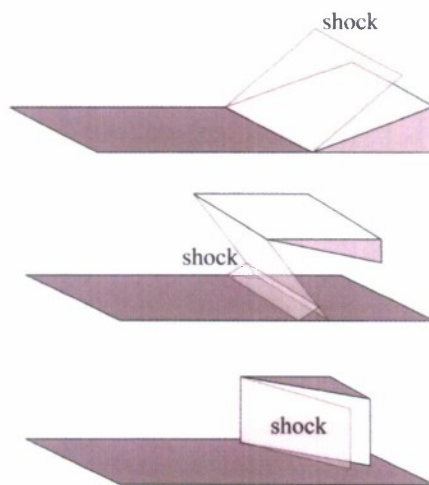
Figure 6: canonical STBLI configurations.
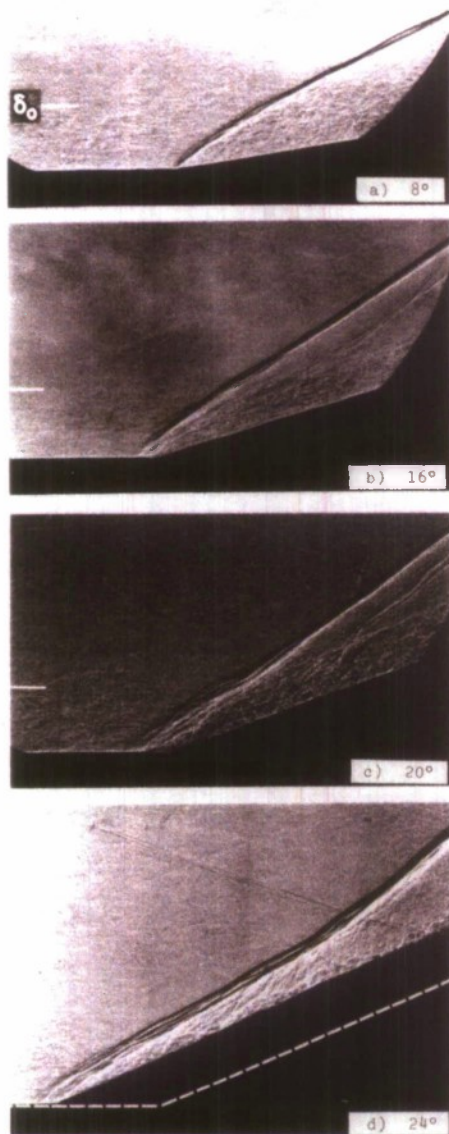
Figure 7: Shadowgraph images of Mach 2.85 compression corner interactions at various wedge angles (Settles et al, 1978)
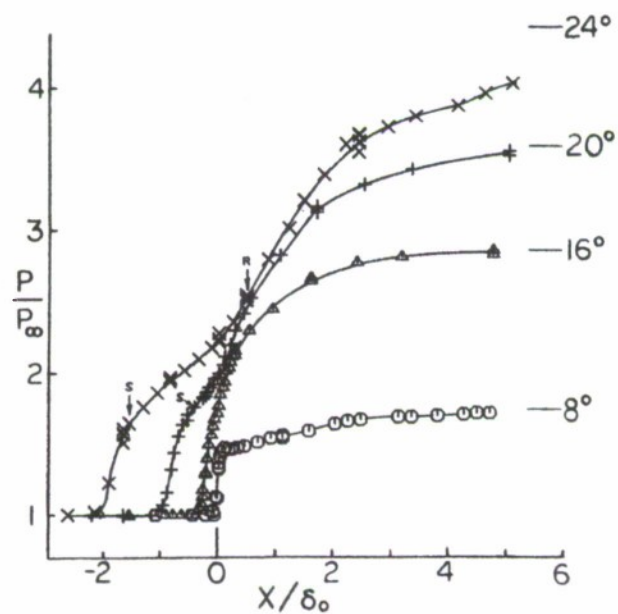
Figure 8: Surface pressure distribution on various compression corner interactions at Mach 2.85 (Settles et al, 1978)

Figure 9: Schematic of an unseparated reflected shock interaction (Delery and Marvin, 1986).

Figure 10: Schematic of a separated reflected shock interaction (Delery & Marvin, 1986).
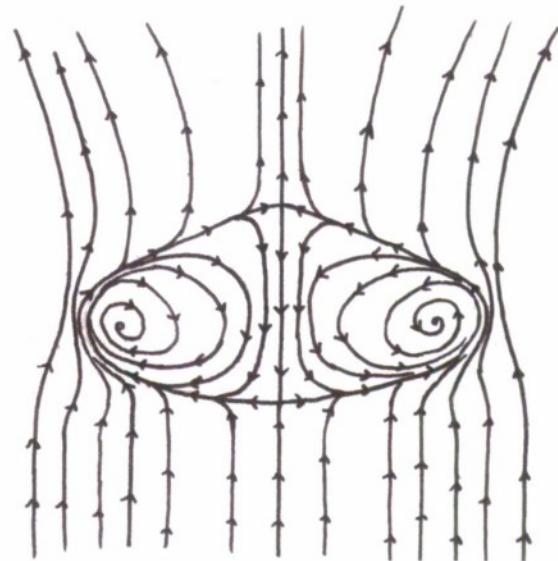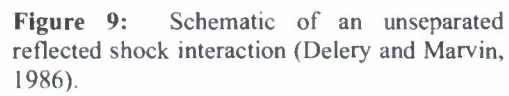
Figure 11: Three-dimensional flow pattern observed experimentally on a reflected shock configuration: (a) surface flow visualization and (b) sketch of the surface streamline pattern, from the experiments of Bookey et al. (2005).
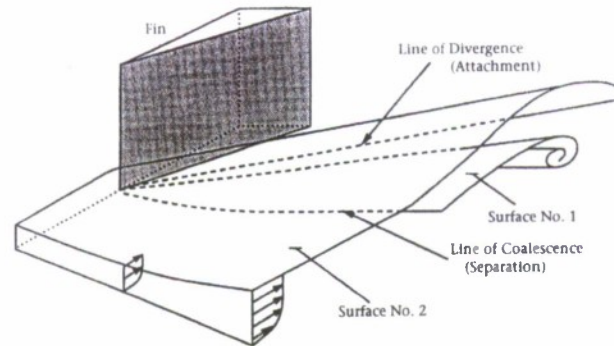
Figure 12: Structure of three-dimensional shock-wave boundary-layer interaction generated by a sharp fin at an angle of attack, from Knight et al. (1987).
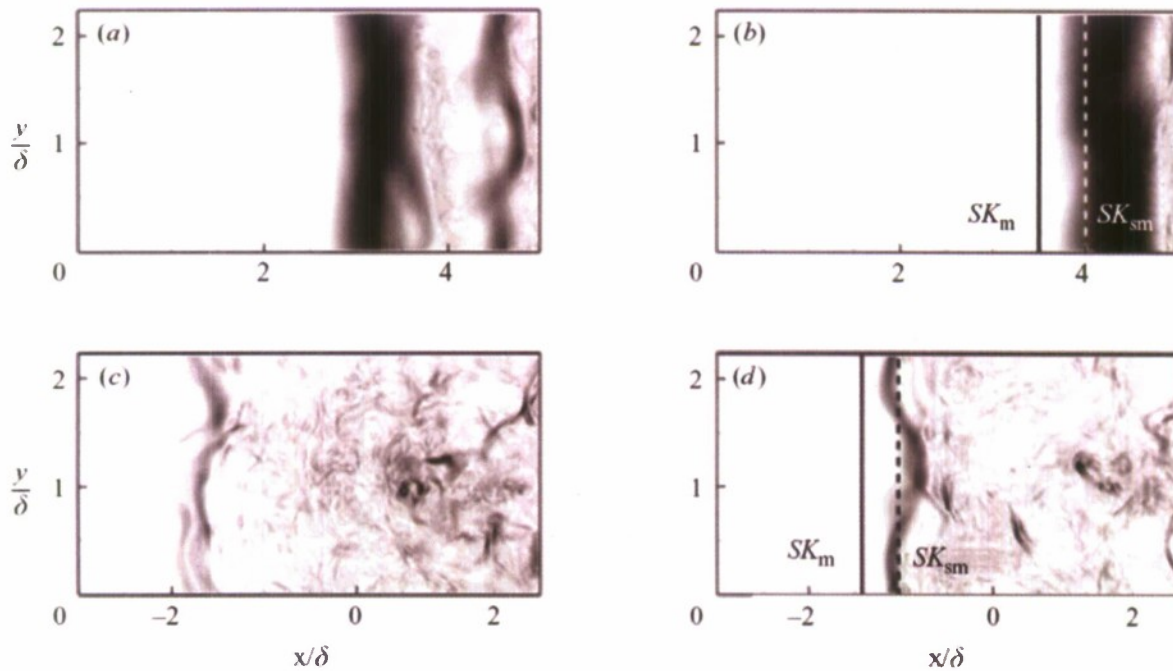
Figure 13: Contours of magnitude of pressure gradient showing the shock location for two flow realizations separated by $50\delta/U_\infty$ at distance from the wall of 2δ (a,b) and 0.9δ (c,d). Dark indicates large gradient. Straight lines indicate the location of the mean shock (SK_m) and the instantaneous spanwise mean shock location (SK_{sm}). From Wu & Martin (2008) using DNS data of a compression corner interaction with incoming boundary layer at Mach 2.9 and Re_θ=2390.
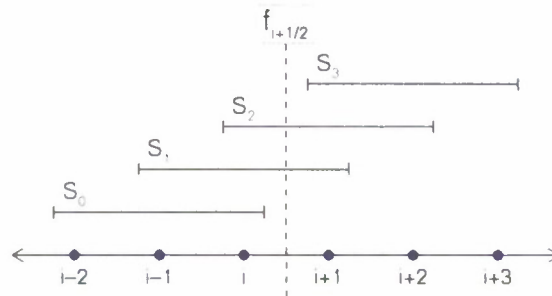
Figure 14: Candidate stencil for the computation of the flux for an $r=3$ $WENO_w$ scheme.
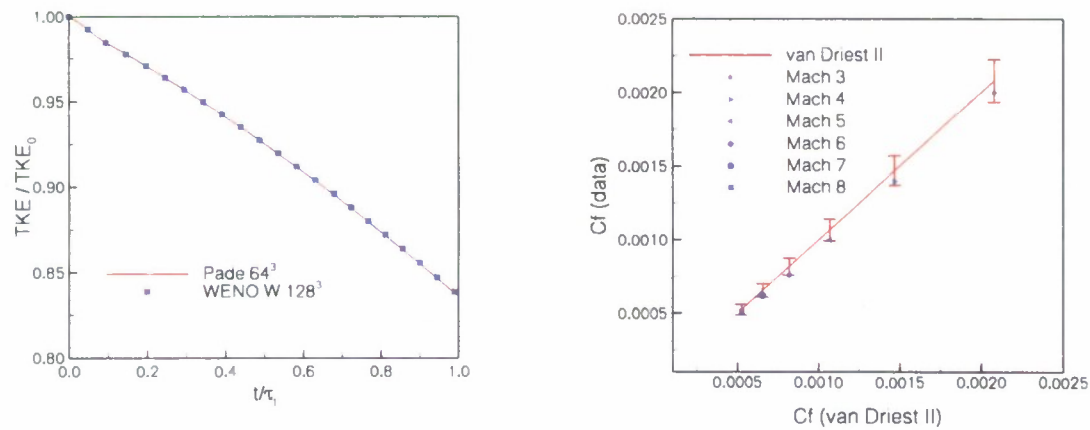
Figure 15: (a) Comparison of DNS data using $WENO_w$ and linear schemes for incompressible isotropic turbulence decay at turbulent Mach number of 0.1 and Reynolds number based on Taylor microscale of 35; (b) DNS data using $WENO_w$ schemes for turbulent boundary layers in the range of Mach 3 to 8 and $Re_\tau = \rho_w u_\tau \delta / \mu_w = 400$ in comparison to van Driest II predictions with error bars at 7%.
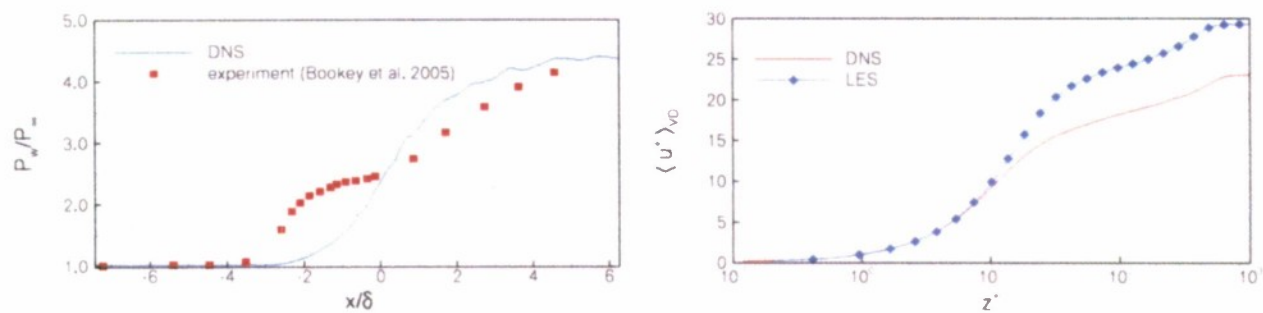
Figure 16: (a) Comparison between DNS data using a WENO$_w$ scheme against experiments at the same conditions for a STBLI in a compression corner configuration. Incoming boundary layer at Mach 3 and Reynolds number based on momentum thickness of 2400. (b) Comparison between DNS and LES data of a turbulent boundary layer at Mach 4 and Reynolds number based on momentum thickness of 9800 using WENO$_w$ schemes.
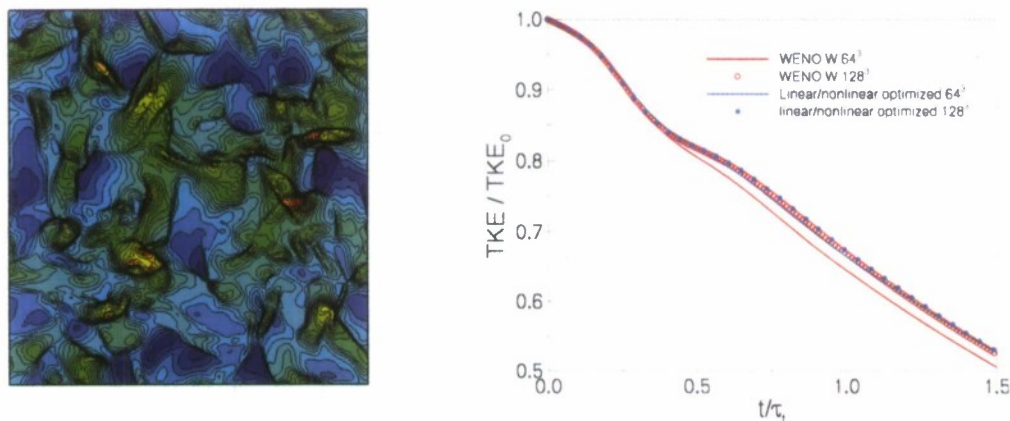
Figure 17: DNS data of decaying isotropic turbulence at turbulent Mach number of 1.5 and Reynolds number based on Taylor microscale of 50. (a) Density gradients showing abundant number of shocklets in the highly compressible turbulence field; (b) Decay of turbulent kinetic energy for WENO$_w$ and linearly/nonlinearly optimized WENO methods at different grid resolution showing grid convergence properties.
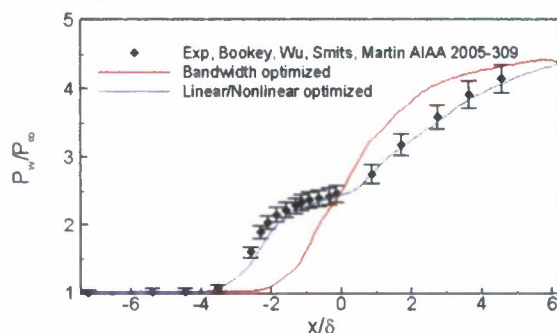
Figure 18: Wall-pressure distribution comparing DNS and experimental data at the same conditions and flow configuration as in Figure 16. DNS solutions for WENO$_w$ and linearly/nonlinearly optimized WENO methods. Experimental uncertainty of 5% shown. From Wu & Martin (2007).
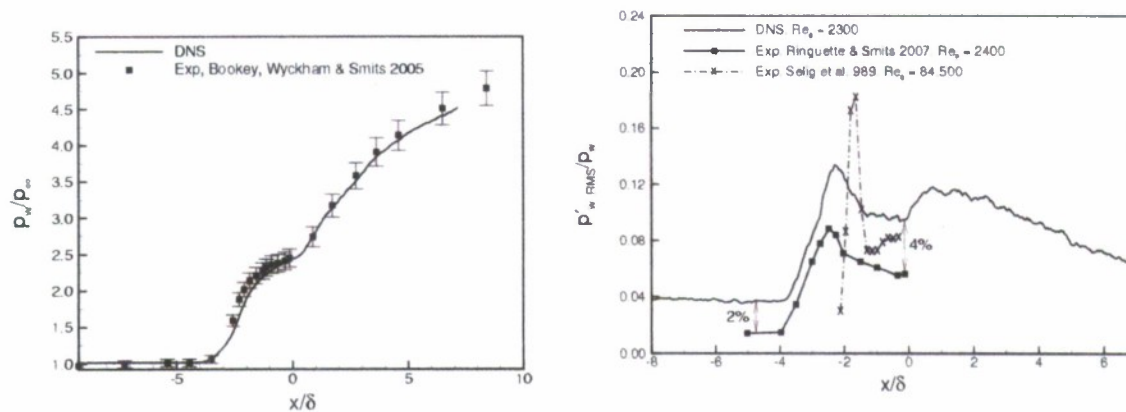
Figure 19: Wall-pressure distribution for the compression corner case with incoming boundary layer at Mach 2.9 and Re_θ=2390 and wall deflection of 24°. (a) Mean from DNS and experiment (adapted from Wu & Martin, 2007) and (b) rms from DNS and experiments (adapted from Ringuette, Wu & Martin, 2008).
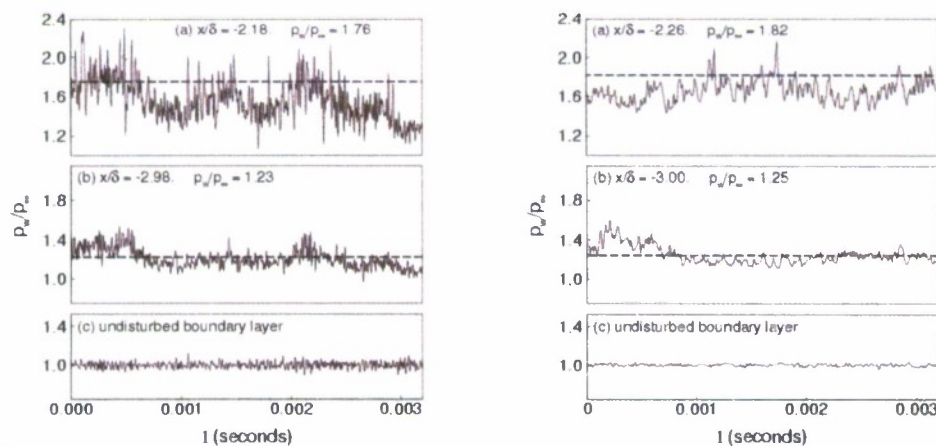
Figure 20: Wall-pressure signal from DNS data at three streamwise locations compared to the experiments at the same flow conditions as Fig 19. (a) DNS signal. The DNS data are low-pass filtered at the same cut-off frequency as the experiments. (b) Experimental data at matching conditions. Dashed lines indicate mean values. Adapted from Ringuette, Wu & Martin (2008).
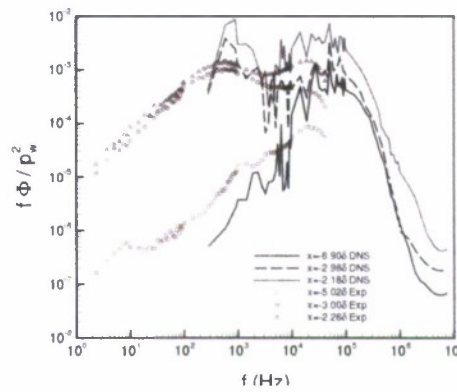
Figure 21: Pre-multiplied energy spectral density of the wall signal at three different streamwise locations for the DNS (lines) and experiments (symbols) at the same flow conditions as in Fig 19. The streamwise locations correspond to the incoming boundary layer, the mean separation point, and the peak in the $p'_{w,RMS}$ curve, respectively. Adapted from Ringuette, Wu & Martin (2008).
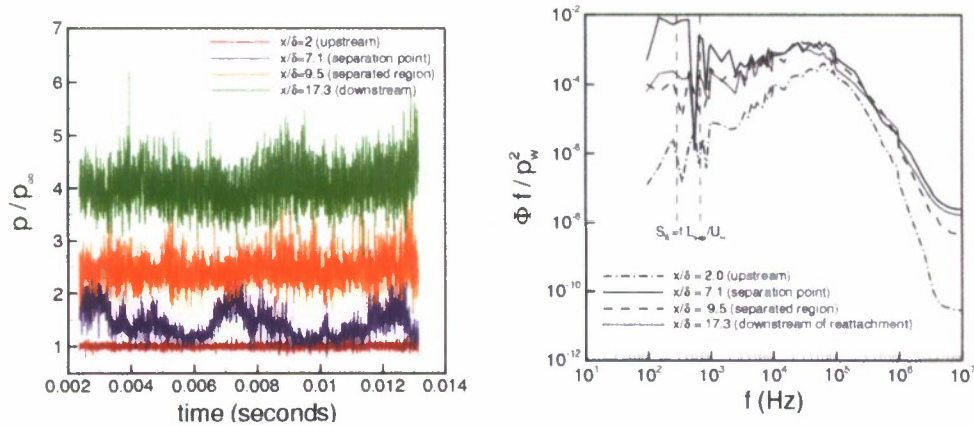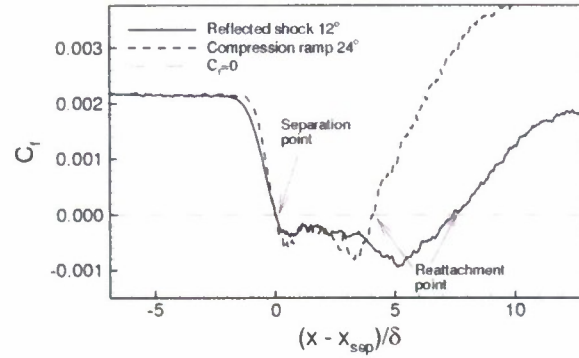

Figure 22: DNS data of a reflected shock configuration with incoming boundary layer at Mach 2.9 and $Re_\theta = 2390$ generated by a $12°$ wedge in the freestream. (a) Wall-presure signal and (b) pre-multiplied energy spectral density for the wall-pressure at different streamwise locations. Adapted from Martin, Priebe & Wu (2008).
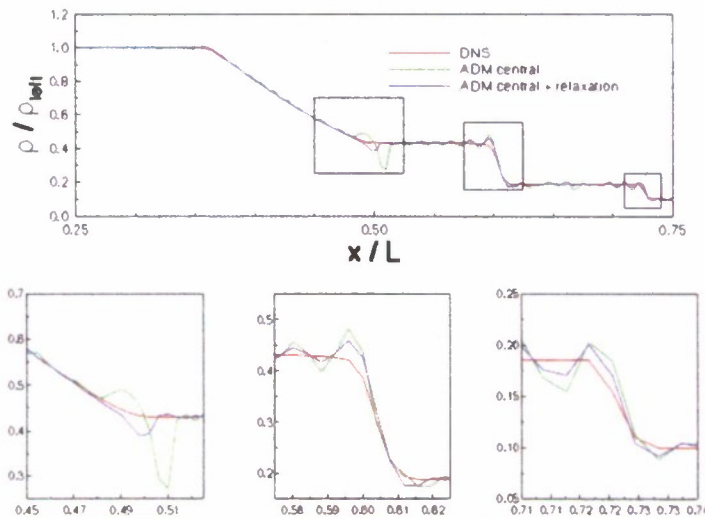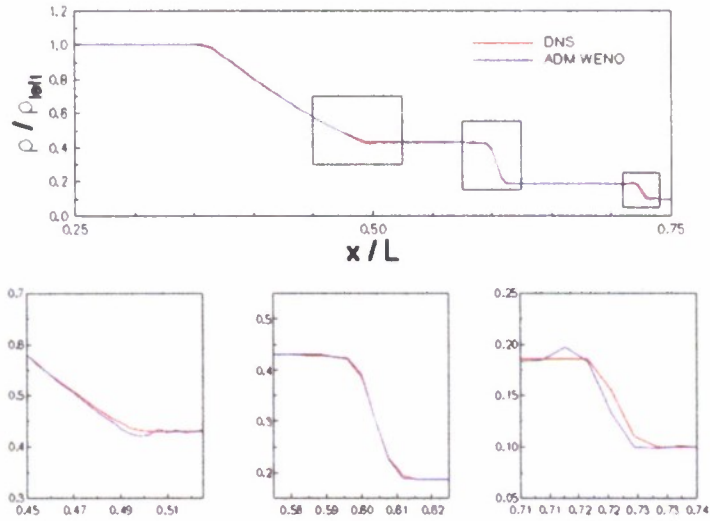
**Figure 23:** Skin friction coefficient from DNS. Adapted from Martin, Priebe & Wu (2008).
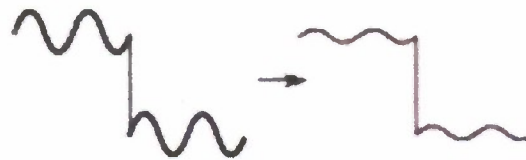
Figure 24: Ideal behavior of a shock-confining filter.

Figure 25: Density profiles in shocktube problem from WENO-based DNS, ADM with central differencing, and ADM with central differencing and regularization. From Grube, Taylor & Martin (2007).

Figure 26: Density profiles in shocktube problem from WENO-based DNS, and WENO-based ADM using a linear tophat filter. From Grube, Taylor & Martin (2007).
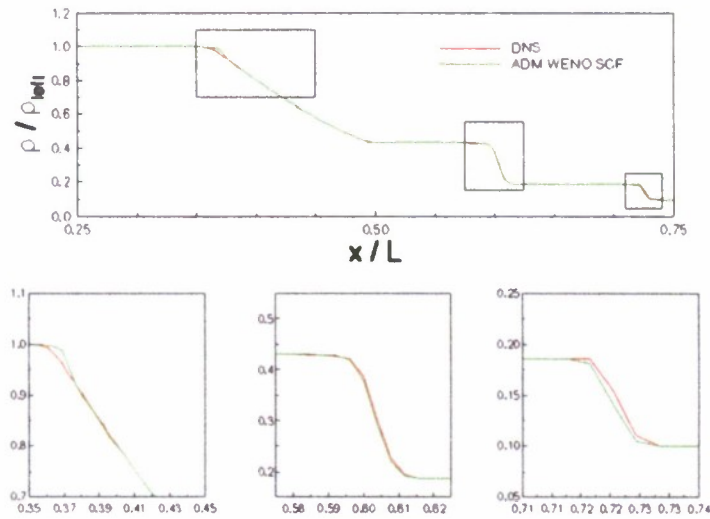
Figure 27: Density profiles in shocktube problem from WENO-based DNS, and linearly and non-linearly optimized WENO ADM using shock-confining tophat filter. From Grube, Taylor & Martin (2007).